Materials Today Chemistry 14 (2019) 100211

Contents lists available at ScienceDirect

Materials Today Chemistry

journal homepage: www.journals.elsevier.com/materials-today-chemistry/

Designing biocompatible and multicolor fluorescent hydroxyapatite nanoparticles for cell-imaging applications

T.R. Machado [a, *], I.S. Leite [b], N.M. Inada [b], M.S. Li [b], J.S. da Silva [a], J. Andrés [c], H. Beltrán-Mir [d], E. Cordoncillo [d], E. Longo [a]

[a] Departamento de Química, CDMF, Universidade Federal de São Carlos (UFSCar), 13565-905 São Carlos, São Paulo, Brazil
[b] Instituto de Física de São Carlos, Universidade de São Paulo (USP), 13560-970 São Carlos, São Paulo, Brazil
[c] Departamento de Química Física I Analítica, Universitat Jaume I (UJI), 12071 Castelló de La Plana, Spain
[d] Departament de Química Inorgànica I Orgànica, Universitat Jaume I (UJI), 12071 Castelló de La Plana, Spain

ARTICLE INFO

Article history:
Received 26 August 2019
Received in revised form
10 October 2019
Accepted 14 October 2019
Available online 13 November 2019

Keywords:
Hydroxyapatite
Bioimaging
Defects
Fluorescence
Chemical precipitation

ABSTRACT

In recent years, there has been a growing effort toward the synthesis, engineering and property tuning of biocompatible nanoparticles (NPs) that can be detected by confocal microscopy and then used as fluorescent probes. Defect-related fluorescent hydroxyapatite (HA) is attracting considerable attention as a suitable material for cell-imaging owing to its excellent biocompatibility, biodegradability, easy cell internalization capability, and its stable and intense blue fluorescence. Although the self-activated fluorescence of HA is advantageous, as it avoids the use of lanthanide dopants, organic dyes, or the need to be combined with other fluorescent inorganic nanocrystals, its preparation by simple procedures with fine control of the defects which govern this property remains challenging. In this study, we propose a new, simple, and cost-effective strategy of fluorescence imaging using HA nanorods (HAnrs) obtained by chemical precipitation followed by heat treatment at relative low temperature (350°C) without using any sophisticated equipment or inorganic/organic additives. Structural, compositional, and morphological analysis, as well as a cytotoxicity assay, are described in detail. The fluorescence characterization of HAnrs shows an intense bluish-white broad-band emission (λ_{max} = 535 nm), and the defects which cause this behavior are studied by temperature-dependent photoluminescence measurements (38–300 K). Moreover, the high density of defects in heat-treated HA leads to tunable fluorescent property (λ_{max} = 399–650 nm) across the entire visible spectrum as a function of the excitation wavelength (λ_{exc} = 330–630 nm) with the potential for further multicolor imaging applications. Labeling results by confocal microscopy show that HAnr co-cultured with human dermal fibroblast cell line exhibit fluorescence signals in the cells even after 48 h of incubation with no evident cytotoxic effects. Therefore, heat-treated fluorescent HAnr can be utilized for tracking and monitoring cells and is a safe alternative for the traditional probes used in bioimaging procedures.

1. Introduction

Fluorescence imaging (or simply bioimaging) is one of the most common methods in bioscience for specific and high-resolution imaging of biological matter. This is a versatile, non-invasive, and low-cost technique which provides detailed information on biological structures and intracellular events with enhanced contrast [1]. The principle for imaging is based on making samples or cells fluorescent from the emitted signal of probes composed of (i) common fluorophores, fluorescent proteins, and lanthanide complexes or (ii) fluorescent systems based on biocompatible nanoparticles (NPs) [2]. Fluorescent probes can significantly improve the effectiveness of diagnosis and therapeutic procedures, such as by the association of imaging and chemotherapy of metastatic tumor cells [3]. In special, there is a vast list of fluorescent NPs which can be internalized into cells for specific intracellular imaging procedures, including those comprised of polymers [4], up- and down-converting inorganic nanocrystals [5–7], carbonaceous materials [8,9], noble metals [10,11], or their combination in sophisticated nanoarchitectures [12–14]. Their surface chemistry can

* Corresponding author.
E-mail address: tmachado.quimica@gmail.com (T.R. Machado).

https://doi.org/10.1016/j.mtchem.2019.100211
2468-5194/

also be modified if targeted imaging or biosensing/imaging is desired [15,16]. For instance, carbon nanotubes with surface functionalization sneak into and out of cells to extract molecules for cellular analysis, and the process can be monitored by fluorescence imaging [17]. NP-based fluorescent systems have experienced unprecedent success in imaging because of several advantages over common probes, such as improved brightness, inertness to distinct microenvironments, and robust photostability with improved resistance to photobleaching. Also, they do not decompose under repeated excitation processes [18].

Among the large variety of nanostructured materials available for bioimaging, fluorescent Ca-based systems have attracted increasing interest and are considered a safe substitute for inorganic NPs with poor degradability and potential long-term toxicity [19]. One of the most studied systems for this purpose is hydroxyapatite (HA), which belongs to the family of calcium orthophosphates. HA has the general formula $Ca_{10}(PO_4)_6(OH)_2$ and typically crystallizes in hexagonal symmetry with the $P6_3/m$ space group [20]. As the material most similar to the mineral phase of hard tissues (labeled as bioapatite), synthetic HA bioceramic is traditionally considered ideal for tissue engineering and bone repair [21–23]. HA NPs are currently being extensively studied for future clinical and biomedical trials in theranostics applications owing to their superior biocompatibility, tunable biodegradability, and pH-dependent solubility, as well as their relatively easy preparation, functionalization, and drug/gene loading capability [24–27]. However, the low intrinsic optical response of HA NPs is an important research challenge for fluorescence imaging.

To avoid this drawback, HA-based materials for cell imaging can be activated by combining them with organic fluorophores [28–30], doping the matrix with lanthanide ions [31–37] or by manufacturing composites with other inorganic nanomaterials such as carbon-quantum and chalcogenide-quantum dots and $Na(Y/Gd)F_4:Yb^{3+}Er^{3+}$ nanocrystals [38–40]. Although these approaches can solve this problem, new difficulties related to these contrast agents could potentially arise, *e.g.* organic dyes typically suffer from lack of photostability and are prone to photobleaching [41]. In addition, HA is composed of abundant and non-expensive elements, but the incorporation of lanthanides leads to a costly final material; the safety of lanthanide-containing systems and quantum dots are also often questioned, limiting *in vivo* applications [42,43].

In parallel to the aforementioned efforts, the strategy of manipulating intrinsic defects and impurities can be used to improve the optical properties of materials [44]. This approach is gaining attention for the generation of low-cost and biocompatible systems with intense and tunable fluorescent emissions for bioimaging procedures [45]. Exploring HA NPs for this purpose is advantageous, because of a unique structural arrangement that is capable of supporting significant lattice distortions. Countless foreign species or impurities of almost any size and valence state (such as SiO_4^{4-}, As^{5+}, or organic molecules) can be stabilized without collapsing the crystal symmetry [46]. In fact, pure and stoichiometric HA with hexagonal structure virtually never occurs, and impurities (CO_3^{2-}, H_2O, etc.) and vacancies (Ca, OH vacancies) are present in almost all cases for the stabilization of this phase [47].

The engineering of these species during the synthesis and processing of HA can regulate its final properties and can lead to an intrinsic broad-band fluorescence with a maximum in the blue region (λ_{max} = 395–420 nm) useful in theranostic applications without lanthanide doping or fluorophore loadings [48–52]. In general, for these biomedical approaches, intrinsically fluorescent HA NPs are prepared by a hydrothermal route using organic molecules (such as trisodium citrate, hexadecyltrimethylammonium bromide, L-aspartic acid monomer, or polyethylene glycol), which decompose and allow the fluorescence to be improved by the incorporation of a $CO_2^{\bullet-}$ impurity [49,50,53]. More recently, *Deshmukh* et al. [54] synthesized self-activated fluorescent HA NPs with a maximum at 530 nm (blue/green region) with a modified sol-gel method using various protocols and stabilizing agents (triethyl amine and acetyl acetone) and solvents (water and dimethyl sulfoxide). The fluorescence attributed to surface energy states in the NPs was proved by uptake in both prokaryotic and eukaryotic cells, confirming the excellent intracellular imaging capability of HA.

Another way to activate defective luminescent materials is by thermal annealing at relatively low temperatures of chemically precipitated samples, with the important advantage of avoiding the use of solvents or complex organic modifiers [55,56]. In recent work, our research group has demonstrated a novel methodology where the precise control and manipulation of the defective energy states and impurities trapped in the lattice is possible depending on the heating temperature (90–800°C), leading to new range of tunable visible broad-band emissions from bluish to yellowish white light (λ_{max} = 440–620 nm) in HA nanorods (HAnrs). Such behavior was further reinforced by the findings of *Gonzalez* et al. [57].

The question that now arises is whether the intrinsic fluorescence of the HAnrs is suitable for biomedical approaches. Herein, the main goal is to obtain a new activator-free or dye-free HA compound. To this end, first we want to provide insight into the structural and optical properties of HAnrs to understand the origin of the emissions, including low-temperature fluorescence measurements and the full-tunable behavior depending on excitation wavelength and excitation sources. Second, we want to know if these self-activated fluorescent HA NPs are efficiently internalized by human cells, for intracellular imaging purposes.

2. Materials and methods

2.1. Materials

Calcium nitrate tetrahydrate ($Ca(NO_3)_2.4H_2O$, 99%) and diammonium phosphate ($(NH_4)_2HPO_4$, 98+%) were purchased from Sigma Aldrich and Strem Chemicals, respectively. Ammonium hydroxide and absolute ethanol were both purchased from Labsynth. All reagents were used as received without further purification. Milli-Q water was used in all experiments. Human dermal fibroblast neonatal (HDFn, catalog number C0045C) cell line was purchased from Thermo Fischer Scientific and was cultivated with Dulbecco's Modified Eagle's Medium (DMEM, Cultilab, Campinas-SP, Brazil) supplemented with 10% (v/v) fetal bovine serum (FBS, Cultilab, Campinas-SP, Brazil) in a humidified incubator at 37°C under a 5% CO_2 atmosphere. MTT (3-[4,5-dimethylthiazol-2-yl]-2,5-diphenyltetrazolium bromide) was purchased from Sigma-Aldrich, dimethyl sulfoxide (DMSO) from Labsynth, and Alexa Fluor 532 Phalloidin (catalog number A22282) from Thermo Fisher Scientific.

2.2. Synthesis of fluorescent HA NPs

HAnr samples were synthesized *via* chemical precipitation as described in our previously published studies [58,59]. Briefly, 10 mmol of $Ca(NO_3)_2.4H_2O$ and 6 mmol of $(NH_4)_2HPO_4$ were dissolved in 50 and 100 mL of water, respectively. Then, the pH of the resulting aqueous solutions was adjusted to 9.5–10.0 by adding ammonium hydroxide. Dropwise addition of the $(NH_4)_2HPO_4$ solution to the $Ca(NO_3)_2.4H_2O$ solution was performed at an approximate rate of 7 mL/min using a peristaltic pump. The mixture was ripened for 2 h maintaining the temperature at 90°C.

The resulting solid product was recovered and washed thoroughly by centrifugation with water and absolute ethanol to remove all the residual reagents. The resulting powder was dried at 80°C for 24 h in air and is referred to as HAnr sample. The HAnr sample was placed in a programmable furnace and heated from room temperature to 350°C for 4 h at a heating rate of 5°C/min in air for the preparation of highly fluorescent HAnrs. The sample was then naturally cooled to room temperature and is referred to as the HAnr350 sample.

2.3. Characterization of HA NPs

The HAnr and HAnr350 samples were structurally characterized by X-ray diffraction (XRD) in a Shimadzu XRD-6000 (Japan) diffractometer using *Cu Kα* radiation ($\lambda = 0.154184$ nm). Data were collected for 2θ values from 10° to 80° using a step scan rate and step size of 0.2°/min and 0.02°, respectively. Fourier transform infrared (FTIR) spectroscopy was performed using a Jasco FT/IR-6200 (Japan) spectrophotometer operated in absorbance mode. Spectra were recorded at a resolution of 4 cm^{-1} over the wavenumber range 400–4000 cm^{-1}. UV–Vis spectroscopy was performed using a Varian Cary 5G (USA) spectrophotometer operated in diffuse-reflection mode. X-ray photoelectron spectroscopy (XPS) analyses were performed on a Scienta Omicron ESCA+spectrometer (Germany) using monochromatic Al Kα (1486.7 eV). The binding energies of all elements were calibrated by referencing to the C 1s peak at 284.8 eV. The morphological features were examined by field-emission scanning electron microscopy (FE-SEM) with a Carl Zeiss Supra 35-VP (Germany) microscope operated at 5 kV. The NP dimensions were estimated using distinct FE-SEM images collected from the sample heat treated at 350°C. The number of counts required for statistical analyses was 100 NPs. Transmission electron microscopy (TEM) and high-resolution transmission electron microscopy (HR-TEM) micrographs as well as selected area electron diffraction (SAED) and energy-dispersive X-ray spectroscopy (EDS) analyses were performed in a FEI TECNAI F20 (The Netherlands) microscope operating at 200 kV. Thermogravimetric (TG) analysis was performed using a Netzsch TG 209 F1 Iris (Germany) thermo-microbalance from 25°C to 1200°C at a heating rate of 10°C/min under a synthetic air atmosphere (5 mL/min of O_2 and 15 mL/min of N_2). Elemental analysis for C, H, N, and O was conducted in a Leco TruSpec Micro Series (USA).

2.4. Fluorescence of HA NPs

Fluorescence spectroscopy using a high-powered source was conducted at room temperature, applying modulation and lock-in detection using a Thermal Jarrel Ash Monospec 27 (USA) monochromator coupled to a Hamamatsu R955 (Japan) photomultiplier. A Coherent Innova 200 K krypton ion laser (USA) ($\lambda_{exc} = 350$ nm) was used as an excitation source with a power of 500 mW, where the incident laser beam reaches the samples at a maximum power of 14 mW. For the temperature-dependent study, the measurements were conducted through an optical fiber cryogenic probe submersed in liquid helium in a Dewar at the temperature range 300–38 K and using an Ocean Optics QE65000 (USA) spectrophotometer coupled with a CCD Hamamatsu S7031-1006 (Japan) detector. The same excitation source as the one used in the room temperature study was used without modulation, but in this case, the maximum power at the sample was 30 mW. For the fluorescence study with a low power source at distinct wavelengths of excitation, a Horiba Jobin Yvon Fluorolog-3 FL3-122 (Japan) spectrofluorometer was used, coupled with a Xenon lamp source (450 W) and equipped with a Hamamatsu R928 (Japan) detector.

2.5. Biocompatibility probes

To assess the effects of fluorescent HAnr350 on the viability of healthy cells, cultures of HDFn cell line were exposed to the NPs. Briefly, 96-well plates were seeded with 10^5 cells/mL suspensions prepared in DMEM supplemented with 10% FBS (v/v) and maintained for 24 h prior to the assays at 37°C in a humidified incubator under a 5% CO_2 atmosphere. The fibroblasts were exposed to HA NPs solutions of 20–320 μg/mL, freshly prepared (using an ultrasonic bath to redisperse the NPs and overcome aggregation in aqueous media) in phenol-free DMEM supplemented with 10% FBS. Samples were incubated for 24 and 48 h in a humidified incubator, and the cellular viability was assessed indirectly using the MTT assay. Absorbance values were obtained at 570 nm using a microplate spectrophotometer Multiskan™ Go (ThermoFisher Scientific), and the NPs interference was minimized by transferring the DMSO, after formazan solubilization, to a new 96-well plate. Viability values were determined considering the absorbance values of the control group (cells not exposed to HA NPs, 0 μg/mL) as 100% of cell viability. Each experiment was conducted with quintuplicates, and the assays were repeated on two different occasions.

2.6. Confocal probes and cellular uptake of HA

First, the fluorescence signal of the HAnr350 dry powder was directly evaluated by laser scanning confocal microscopy (LSCM) in an inverted Zeiss LSM 780 microscope (Carl Zeiss) coupled with a non-descanned detector. Single-photon excitations were conducted using a Diode laser (405 nm), Ar laser (458, 488, and 514 nm), and HeNe laser (543, 594, 633 nm). In the next step, the internalization of HAnr350 was probed by LSCM. Suspensions of 10^4 cells/mL of HDFn cells, prepared in phenol-free DMEM supplemented with 10% FBS, were seeded in 35 mm cell culture dishes (Ibidi) and incubated for 24 h at 37°C. Cell media were replaced with 320 μg/mL HA NPs and incubated for 48 h. Samples were gently washed twice with phosphate-buffered saline, and the F-actin was stained with Alexa Fluor 532 Phalloidin, labeling cells cytoskeleton, for imaging with the confocal microscope using single-photon excitation (514 nm for Alexa Fluor and 405 nm for HA NPs). The same procedure was used for multicolor intracellular imaging but without cytoskeleton labeling. In this case, the fluorescence of HAnr350 sample was probed using 405, 488, 543, and 594 nm as the excitation wavelengths.

3. Results and discussion

A schematic representation of the results obtained in this work is presented in Fig. 1. By a simple chemical precipitation followed by heat treatment, the fluorescent properties of HA can be greatly improved. Owing to this characteristic, the possibility of tuning the emission colors and the high biocompatibility of the nanorods, they can be used in several applications from technological to biomedical approaches. Here, we demonstrated the use of HAnrs for cell labeling by confocal microscopy using HDFn cells as a model. The NPs are successfully uptaken, and their fluorescence emissions are intense and defined enough to delimitate distinct cell structures.

3.1. Structure and morphology

Both the synthesis methods and the heat treatment conditions could lead to not only distinct phases of calcium phosphate but also the presence of deleterious phases. In the present study, the crystalline phase and the structural long-range order were evaluated by the XRD patterns presented in Fig. 2(a). All diffraction peaks observed in HAnr and HAnr350 samples can be perfectly indexed to

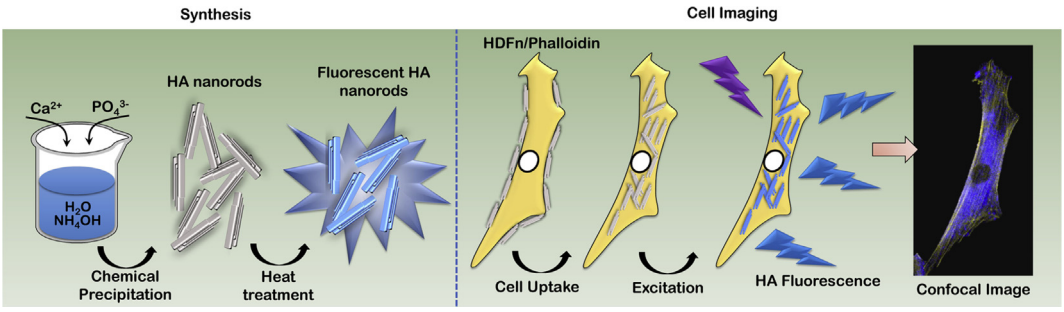

Fig. 1. Schematic of the synthetic route of HA nanorods with improved self-activated fluorescence and their application for cell-imaging. HA, hydroxyapatite.

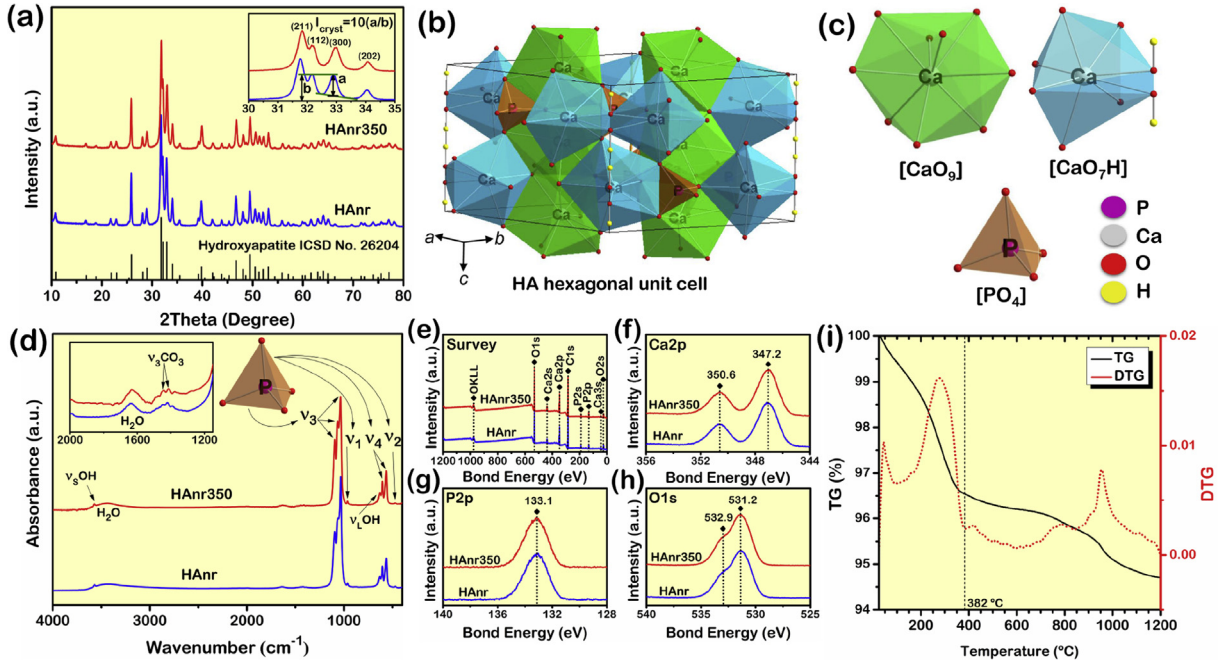

Fig. 2. Structural characterization of HA samples: (a) Lattice ordering at long-range by XRD patterns, (b) representation of HA hexagonal structure, (c) coordination clusters, and (d) lattice ordering at short-range by FTIR spectra. The insets show the calculation of crystallinity index and a magnified view of the ν_3CO_3 region. Surface analysis of HA samples by XPS: (e) Survey, (f) Ca2p, (g) P2p, and (h) O1s; (i) TG analysis of HA sample. HA, hydroxyapatite; FTIR, Fourier transform infrared; XRD, X-ray diffraction; XPS, X-ray photoelectron spectroscopy; TG, Thermogravimetric.

the hexagonal HA phase, in accordance with the results reported in the Inorganic Crystal Structure Data (ICSD) No. 26204 [60]. This phase crystallizes in a hexagonal compact packaging of tetrahedral [PO_4] clusters, with Ca species inserted in the larger cavities formed in the lattice. Fig. 2(b) shows a representation of the HA unit cell, while in Fig. 2(c), the local coordination of each atom, i.e. the constituent clusters of the lattice, is displayed. The 10 different Ca species in the structure are distributed in two distinct sites, labeled as Ca(1) and Ca(2) sites. Ca(1) species are surrounded by nine oxygens belonging to [PO_4] clusters resulting in [CaO_9] clusters. These clusters form the columns in the ternary axes of the structure. The Ca(2) species are surrounded by six oxygens from [PO_4] clusters and one OH group, leading to [CaO_7H] clusters and thus forming the hexagonal channels of the structure [47]. In both samples, well-defined peaks are related to the presence of long-range structural order. This observation corroborates with the degree of crystallinity values found for both samples (8.1 and 7.5 for HAnr and HAnr350 samples, respectively) estimated by the methodology described elsewhere [61], which considers the relative intensities of peaks of the (112) and (300) families of planes (inset, Fig. 2(a)).

Fig. 2(d) shows the FTIR spectra obtained for the HAnr and HAnr350 samples. Vibrational characterization was conducted to further confirm the formation of HA NPs and their thermal stability after annealing. The observed modes are the typical ones for HA samples and can be summarized as follows: the bands at 472 (ν_2), 563, and 605 cm^{-1} (ν_4), 962 cm^{-1} (ν_1), 1033, 1062, and 1098 cm^{-1} (ν_3) are related to distinct vibrational modes of [PO_4] clusters in the HA structure; the bands at 633 and 3570 cm^{-1} arise from librational (ν_L) and stretching (ν_S) modes of OH groups in the hexagonal channels formed in the HA lattice [62]. These bands are relatively well-defined, indicating the existence of short-range structural order in our NPs. The bands at 1620 and 3500 cm^{-1} are associated with physisorbed water. On the other hand, the presence of entrapped impurities in the lattice can also be qualitatively confirmed by FTIR. In this sense, bands at 1421 and 1452 cm^{-1} in both samples are associated with vibrations of structural CO_3 groups (ν_3) substituting OH (A-type) and PO_4 (B-type) groups (inset, Fig. 2(d)) [63]. Very weak bands (not shown) are also observed between 870 and 890 cm^{-1} which could be associated

with AB-type CO_3 substitution as well as the presence of entrapped NH_4^+ groups substituting Ca atoms [58,64].

In the present study, we also performed XPS analysis of the HA samples to evaluate their chemical composition and surface valence states. Fig. 2(e) shows the survey spectra of all samples. The presence of the main binding-energy peaks of Ca (2s, 2p, 3s), P (2s, 2p), and O (*KLL*, 1s, 2s) confirms the presence of the main elements which make up the HA structure. Moreover, a peak related to C (1s) is also observed in both samples, which could be associated with CO_3^{2-} in our samples. The high-resolution XPS spectra of Ca in Fig. 2(f) shows peaks at 350.6 and 347.2 eV ascribed to the characteristic binding energies of $Ca2p_{1/2}$ and $Ca2p_{3/2}$ doublets, respectively, caused by spin-orbit coupling in divalent Ca. Fig. 2(g) shows the high-resolution spectra for P, where the P 2p peak observed at 133.1 eV corresponds to the binding energy of pentavalent P inserted in [PO_4] clusters of the HA structure [65]. The spectra for O(1s) reveal an asymmetric peak with two components at binding energies of 532.9 and 531.2 eV (Fig. 2(h)). The first peak can be assigned to the O–C bond of structural CO_3 and adsorbed water, and the latter peak is assigned to O at structural OH and PO_4 groups [65,66]. The C 1s spectra (Fig. S1) present three main peaks at 288.6, 285.8, and 284.7 eV, which are normally assigned respectively to CO_3 groups of the HA structure, aliphatic carbon atoms, and α-carbon atoms, which could be associated with carbon pollution from the XPS instrument [66].

To gain a deeper insight into the composition and the presence of trapped species in the HA lattice, an elemental analysis was conducted of the HAnr sample. The results show that the N, C, O, and H contents are 0.10, 0.20, 0.49, and 5.24 wt%, respectively, which suggest the presence of impurities made up of these elements, such as CO_3^{2-}, NH_4^+, and H_2O. To further characterize the composition and thermal behavior of the HAnr sample, we performed a TG analysis, and Fig. 2(i) illustrates the obtained results. The TG curve show a total 5.3 wt% mass loss of HAnrs heated to 1200°C, which can be divided into specific ranges as follows. First, an important mass loss of 3.5 wt% is observed in the RT–382°C range (Fig. 2(i), black dotted line), where a broad and intense peak at the derivative thermogravimetric (DTG) profile is observed because of the occurrence of distinct processes in the HA samples by heating. They are well-reported to correspond to the liberation of adsorbed/lattice water and entrapped NH_3 molecules [67]. The intermediate region at 382–900°C exhibits a 0.9 wt% mass loss with low intensity peaks in the DTG, associated with several processes of degradation of carbonate groups of A-type and B-type substitution, confirming their presence in the HA lattice and posterior decomposition [68]. Finally, the 0.9 wt% mass loss at the high temperature region above approximately 900°C is mainly associated with the continuous process of dehydroxylation of the HA matrix [69].

The morphological aspects of the HA NPs were evaluated by electron microscopy. Fig. 3(a) shows a FE-SEM image for the HAnr350 sample, and HA NPs with a rod-like shape are observed. The size of the NPs was estimated as represented in the inset, and the results are shown in Fig. 3(b) and (c). The HA width and length fit well with a normal Gaussian distribution. Most of the HAnr have widths in the range of 70–80 nm, while their lengths are 300–500 nm in the sample. Fig. 3(d) shows a TEM image of the HAnr350 sample, also illustrating that the sample is composed of only nanorods, and the results in Fig. 3(e) confirm *via* EDS characterization that this region is mainly composed of Ca, P, and O elements, with the presence of the C element assigned to the carbon film of the TEM grid. The results of SAED analysis (Fig. 3(f)) indicate the presence of several concentric rings associated with distinct crystallographic planes of the hexagonal HA phase [60]. A TEM image of a single HAnr is illustrated in Fig. 3(g), and the HR-TEM characterization of this NP is shown in Fig. 3(h). The distance between the crystallographic planes was measured, affording a value of 0.34 nm, which could be indexed to the interplanar distance of the (002) family of planes in HA.

Despite the high degree of crystallinity observed by XRD analysis, the presence of impurities (H_2O, CO_3^{2-}, NH_4^+) is evidenced by FTIR, XPS, elemental analysis, and TG results in the HAnr sample. The presence of CO_3^{2-} by substituting the PO_4^{3-} and OH^- groups takes place *via* a charge compensation mechanism, thus leading to vacancies (Ca, OH), incorporation of other impurities (NH_4^+), and deformations of the lattice [47,67]. Precipitated HA also contains OH vacancies related to crystal disorder [46]. As an effect, defects involving structural distortions in O–Ca–O and O–P–O bond angles and Ca–O, P–O bond lengths can feasibly occur. Moreover, as evidenced by the TG results, our HAnr350 sample which was heat treated at 350°C is at the limit of the first/second regions of mass loss, related to significant lattice water and NH_3 liberation. Water molecules in pores, cracks, intercrystalline locations, and substituting OH groups as well as NH_4^+ groups are irreversibly lost by heating in these conditions [68,69]. At this temperature, a partial decomposition of CO_3^{2-} can also feasibly occur. Several structural changes are associated to these mechanisms, which include variations in *a* and *c* unit cell parameters and cell volume, leading to a significant contraction of the HA structure at the heat treatment temperature of 350°C [58]. This behavior can promote an intensification of the atomic interactions in HA, and consequently, the oscillator strength increases, leading to higher probability of radiative electronic transitions. Hence, the structural rearrangement in the heat-treated material can improve its fluorescent properties.

3.2. Fluorescent properties of HA NPs

Although the HA possesses a high band-gap energy (*Eg*) value, intense fluorescence by excitation in the UV region and at most part of the visible spectrum is possible. It is well known that stoichiometric and ordered HA is not a good fluorescent material, and Ca^{2+} and PO_4^{3-} ions do not emit fluorescence by themselves. Also, in an ordered HA, the density of defective levels is minimized, suppressing the intragap radiative decay (Fig. 4(a)). However, in disordered HA a series of energy levels can be found in the forbidden zone responsible for e'–$h^\bullet$ pair recombination [70], and various experimental/theoretical studies have demonstrated that new optically active levels in the forbidden region of HA occur by the presence of vacancies (such as Ca and OH) [71–73]. On the other hand, lattice carbonates were also observed to follow important rules for the fluorescence of precipitated HA [74], heat-treated synthetic HA [57], and biomimetic apatite [75]. Hence, based on the present study and our recent publications [58,59], we propose that the defect-related fluorescence properties in HAnr sample originate from e'–$h^\bullet$ radiative recombination between defective energy levels because of the non-stoichiometric nature of the structure allowed by the chemical precipitation methodology adopted. This intrinsic nature of hexagonal HA leads to a disordered state as summarized by the broad band model in Fig. 4(a), which displays several vacancies (Ca, OH) and impurities (CO_3^{2-}). These defects, together with other impurities (NH_4^+, H_2O), also affect the electronic densities of [PO_4], [CaO_9], and [CaO_7H] structural clusters by inducing distortions (also associated with the crystallization process of the NPs). The density and equilibrium of these defects and distortions can be manipulated with heat treatment in the HAnr350 sample, which greatly intensifies the electron-hole (e'–$h^\bullet$) recombination process at 350°C by extra disorder in the lattice as a result of the elimination (NH_4^+, H_2O) and partial decomposition (CO_3^{2-}) of impurities. All these factors could result in the

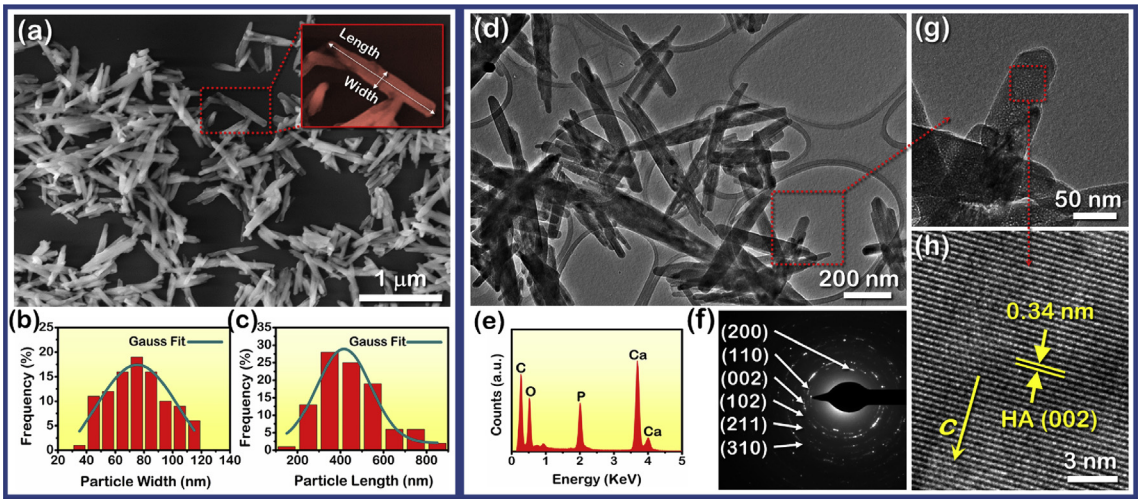

Fig. 3. Morphological characterization of HAnr350 sample. (a) FE-SEM image of HA nanorods and a magnified view of a single nanorod (inset), (b) estimation of particle width, and (c) estimation of particle length. Crystallographic and morphological characterization by TEM (d) low magnification TEM image, (e) EDS analysis, (f) SAED analysis, (g) high magnification TEM image, and (h) HR-TEM image. HA, hydroxyapatite; TEM, transmission electron microscopy; SAED, selected area electron diffraction; FE-SEM, field-emission scanning electron microscopy; EDS, energy-dispersive X-ray spectroscopy; HR-TEM; high-resolution transmission electron microscopy.

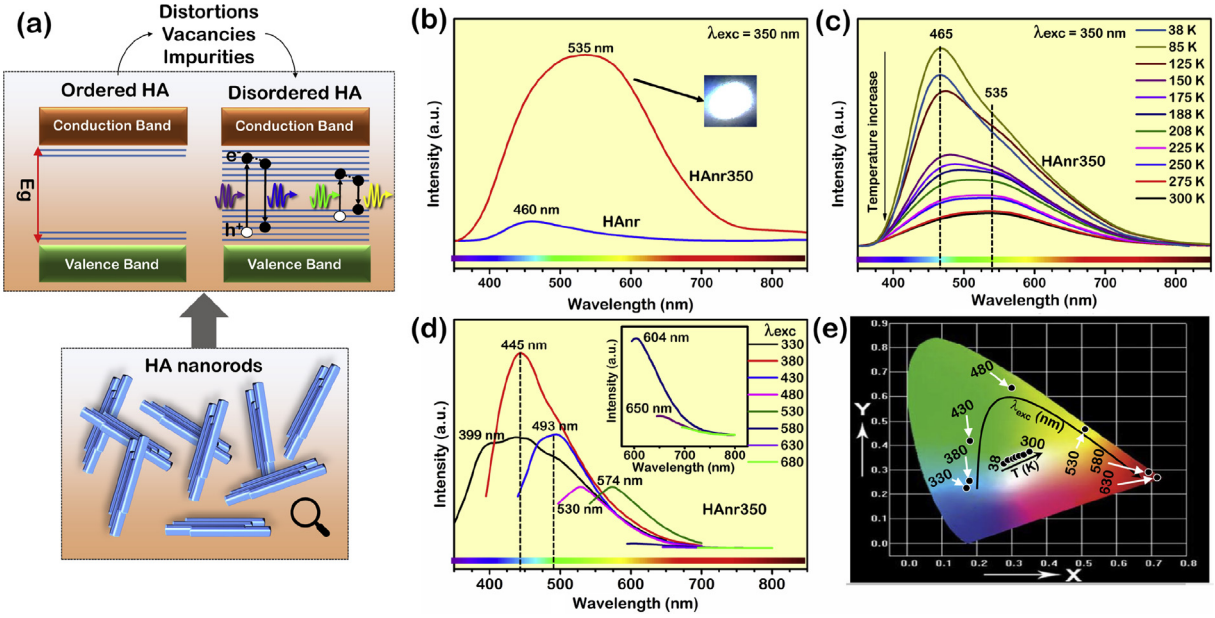

Fig. 4. Optical behavior of HA NPs. (a) General model for the occurrence of self-activated fluorescence in HAnrs. In an ideal ordered HA system, the energy levels in the forbidden zone are minimized. However, the presence of defects and the elimination of impurities causes a higher disorder in HA system which allows radiative recombination of *e'–h•* pairs at defect energy levels between the VB and CB. (b) Emission spectra of HAnr and HAnr350 samples by laser excitation at $\lambda_{exc} = 350$ nm, (c) temperature-dependent photoluminescence of HAnr350 sample by laser excitation at $\lambda_{exc} = 350$ nm, (d) excitation dependence of HAnr350 sample probed by the spectrofluorometer at room temperature, and (e) CIE chromaticity diagram. HAnr, HA nanorod; HA, hydroxyapatite; NP, nanoparticle; VB, valence band; CB, conduction band; CIE, Commission Internationale de l'Éclairage.

fluorescence emissions in HA and its large excitation capability, but it is a hard task to point out the principal defects responsible for fluorescence, as they occur concurrently.

In this section, we have employed several characterization techniques corroborate with the aforementioned discussion on the optical properties of HA NPs. Depending on the characteristics of the irradiation source for the excitation of the matrix, such as power and energy as well as the temperature used to conduct the experiments, distinct energy levels can participate in the *e'–h•* radiative recombination process in materials containing high densities of defective levels [54,76]. Then, distinct aspects of the fluorescence properties are revealed, which also lead to changes in shape, amplitude, and intensity of the emission bands. This kind of study can help to better elucidate the electronic distribution of defect and impurity centers as well as to obtain tunable colors in the same material. Fig. 4(b) shows emission spectra for both HAnr and HAnr350 samples excited at 350 nm (3.54 eV) by a high-power Kr laser source. The spectra are dominated by broad band emissions typical of radiative recombination pathways governed by countless energy levels. For the HAnr and HAnr350 samples, the maxima of the bands are centered at 460 (2.69 eV) and 535 nm (2.31 eV), respectively, although they cover a large part of the visible part of the electromagnetic spectrum. As was discussed in our previous work [58], it is important to note that the UV–Vis spectra obtained for both samples (Fig. S2 and the experimental procedure in the SI file) reveal the presence of emissions with lower energies than the *Eg* of these samples (5.48–5.57 eV), which

are also inferior to the excitation energy (3.54 eV for 350 nm). This result confirms the high contribution of energy levels between forbidden regions for the fluorescence of HA NPs. HA is considered a wide band gap p-type semiconductor, and its optical characteristics are mainly determined by the complex electronic structure of various occupied/unoccupied localized energy states between the valence band (VB) and conduction band (CB) departing from the bulk and surface states [70].

It should be pointed out that the emission intensity is 11 times greater after the heat treatment (HAnr350) procedure following chemical precipitation (HAnr), confirming success in obtaining highly fluorescent HA NPs by this strategy. Moreover, a shift of the emission maximum to a lower wavelength region is observed after the heat treatment. This behavior is accompanied by an enlargement of the band amplitude, yielding a bluish-white emission from the HAnr350 sample (digital image in Fig. 4(b)) because a more homogeneous part of the spectrum is covered by the emission band in this case. This result could be associated with the increase of structural disorder as a consequence of the decomposition and elimination of impurities, enhancing the total density of e'–$h^{\bullet}$ radiative recombination events, in particular those involving shallow defective levels [58]. Hence, the following discussions focus on the HAnr350 sample with improved fluorescence.

In the next step, we studied the fluorescence of HA as a function of temperature. Temperature-dependent photoluminescence (TDPL) is an effective and powerful optical technique which can help to better elucidate the fluorescent mechanism of emitting centers from disordered materials. The electronic recombination processes were studied under conditions of low thermal energy, and by this analysis, the role of thermal vibration in radiative transitions becomes more evident [77]. Fig. 4(c) shows the TDPL spectra for HAnr350 samples from 38 K to room temperature for excitation with a Kr laser at 350 nm. By the present results, a reduction in emission intensity was observed by raising the temperature, which became faster above 125 K. This behavior is associated with thermal quenching, where non-emissive centers become thermally activated at the e'–$h^{\bullet}$ recombination pathways, partially suppressing radiative emissions [78].

Using this technique, it is revealed that the emission spectrum of the HAnr350 sample excited by a laser source is actually composed of at least two main well-defined bands centered at 460 and 535 nm because of the fine structure of these emission bands at low temperatures. The first one matches well with the maximum intensity of the HAnr sample emission band without heat treatment, analyzed at room temperature (Fig. 4(b)); the second less energetic chromophore centered at 535 nm causes a widening of the emission spectrum of the HAnr350 sample and could be associated with a higher occupation of shallow levels in this sample as an effect of the heat treatment methodology. By raising the temperature of TDPL analysis, the intensity of both bands of the HAnr350 sample decreases, but with different behavior, i.e. a higher rate of decrease is observed for the 460 nm band than for the 535 nm band. This causes a shift of the emission band to regions of lower energy and is related to redistribution of charge carriers at the distinct main emissive centers. A possible reason for this behavior is that when an electron occupying levels near the VB is excited to more energetic levels near the CB, it does not recombine with holes to give an emission at 465 nm, but the thermal energy provided by raising the temperature partially dissipates the energy of this electron as lattice phonons. Then, a charge transfer process between defective centers takes place, where the electron is trapped at the less energetic excited states and then experiences radiative decay at the emissive levels responsible for the emission band centered at 535 nm.

In accordance with the results presented by *Deshmukh* et al. [54], the fluorescence monitored by varying the temperature does not reveal any new peaks, and only an increase in intensity of the existing bands is observed, demonstrating that no artefacts are responsible for the fluorescence properties of HA. However, the trend observed in our experiments is distinct from those reported by *Deshmukh* et al. [54], i.e. a shift to higher energy regions (from 528 to 502 nm) by increasing the temperature in comparison to our shift to lower energy (from 460 to 535 nm) and the presence of more peaks at the emission band than in our results. This behavior demonstrates that the preparation pathway dictates the final fluorescence response, and the properties of the HA sample synthesized by our methodology are determined by distinct mechanisms. Also, the study conducted by *Deshmukh* et al. [54] used a distinct laser source (He−Cd) and excitation wavelength (325 nm), which also can change the optical properties observed by the TDPL technique.

For some biological and technological applications, it is necessary to use materials with a wide range of optical properties even when using excitation sources of low power. Fig. 4(d) shows the emission spectra obtained for the HAnr350 sample using a spectrofluorometer equipped with a Xe lamp as the excitation source. For this study, distinct excitation wavelengths from 380 to 680 nm at intervals of 50 nm were selected. First, a shift of emission from blue to red was observed because of the disappearance of the short-wavelength components of emission with an increase in the excitation wavelength. At the near-UV excitation wavelengths, the highest intensities and spectral amplitudes of the fluorescence bands are observed displaying maxima of emissions at blue/green regions. Hence, the optimal excitation energy for saturation of the emission intensity was revealed to be between 330 and 430 nm. At least four main peaks are clearly observed at $\lambda_{exc} = 330$ nm (399, 445, 493, and 530 nm), three at $\lambda_{exc} = 380$ nm (445, 493, and 530 nm), and two at $\lambda_{exc} = 430$ nm (493 and 530 nm) with tails extending to long wavelengths, indicating that distinct pathways for e'–$h^{\bullet}$ recombination are present encompassing various intragap levels. In comparison to laser excitation ($\lambda_{exc} = 350$ nm), a slight shift toward lower wavelengths of the emission bands occurs by excitation in the UV region using the spectrofluorometer, which is attributed to a shift of the maxima as well as a sharpening of the band emissions in this case.

We also probed the excitation of our sample at higher wavelengths across the visible spectrum ($\lambda_{exc} = 480$, 530, 580, 630, and 680 nm), successfully obtaining emissions at green, yellow, and red regions in addition to the aforementioned bands centered at blue/green regions, indicating multicolor properties of the HAnrs. In this region of excitation, an almost regular decrease in emission intensity is observed, but the lower energies used for excitation still produce fluorescence. Interestingly, emission response is observed until $\lambda_{exc} = 630$ nm (1.97 eV), where the excitation energy is significantly lower than the *Eg* value (5.57 eV). This shows that not only a large spectral emission range is possible, but also a high density of defective levels of distinct natures in HA leads to a large excitation capability for the sample. Similar tunable behavior depending on excitation wavelength was observed in other materials [76,79], but the presence of tunable fluorescence in HA was often reported to be because of association with other optically active materials during the synthesis step [80].

Fig. 4(e) shows the Commission Internationale de l'Éclairage (CIE) chromaticity diagram for the HAnr350 sample excited with various irradiation sources at distinct temperatures. Tables S1 and S2 in the SI file lists their corresponding x and y coordinates. In laser excitation experiments at 350 nm, the HAnr350 sample displays CIE coordinates localized at the white region color which are close to those related to pure white ($x = 0.33$ and $y = 0.33$). As the

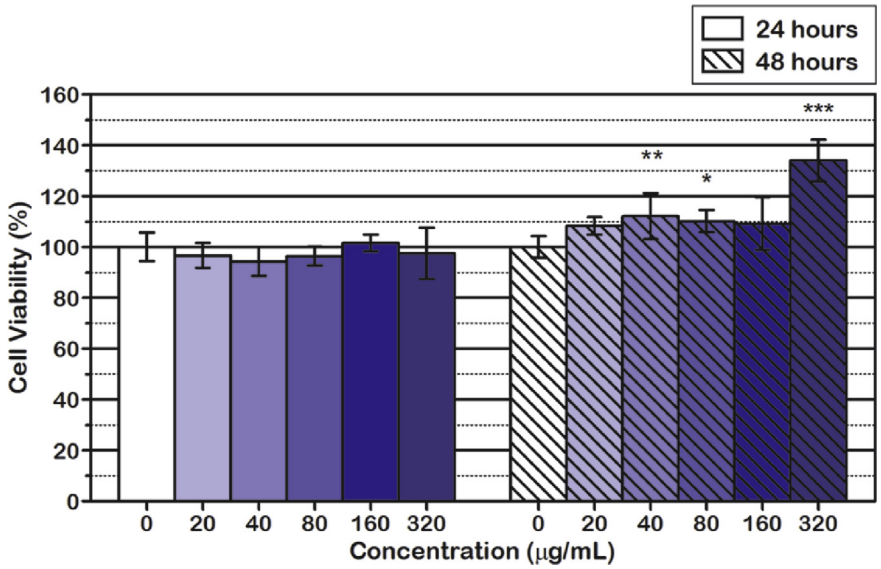

Fig. 5. *In vitro* cell viability by MTT assay of HDFn cell line incubated with HAnr350 sample at distinct dosages (0, 20, 40, 80, 160, and 320 μg/mL) for 24 and 48 h. Groups which demonstrated significant statistical difference are marked with *, **, and *** ($p \leq 0.05$, $p \leq 0.005$, and $p \leq 0.0005$ respectively). HAnr, HA nanorod; HDFn, Human dermal fibroblast.

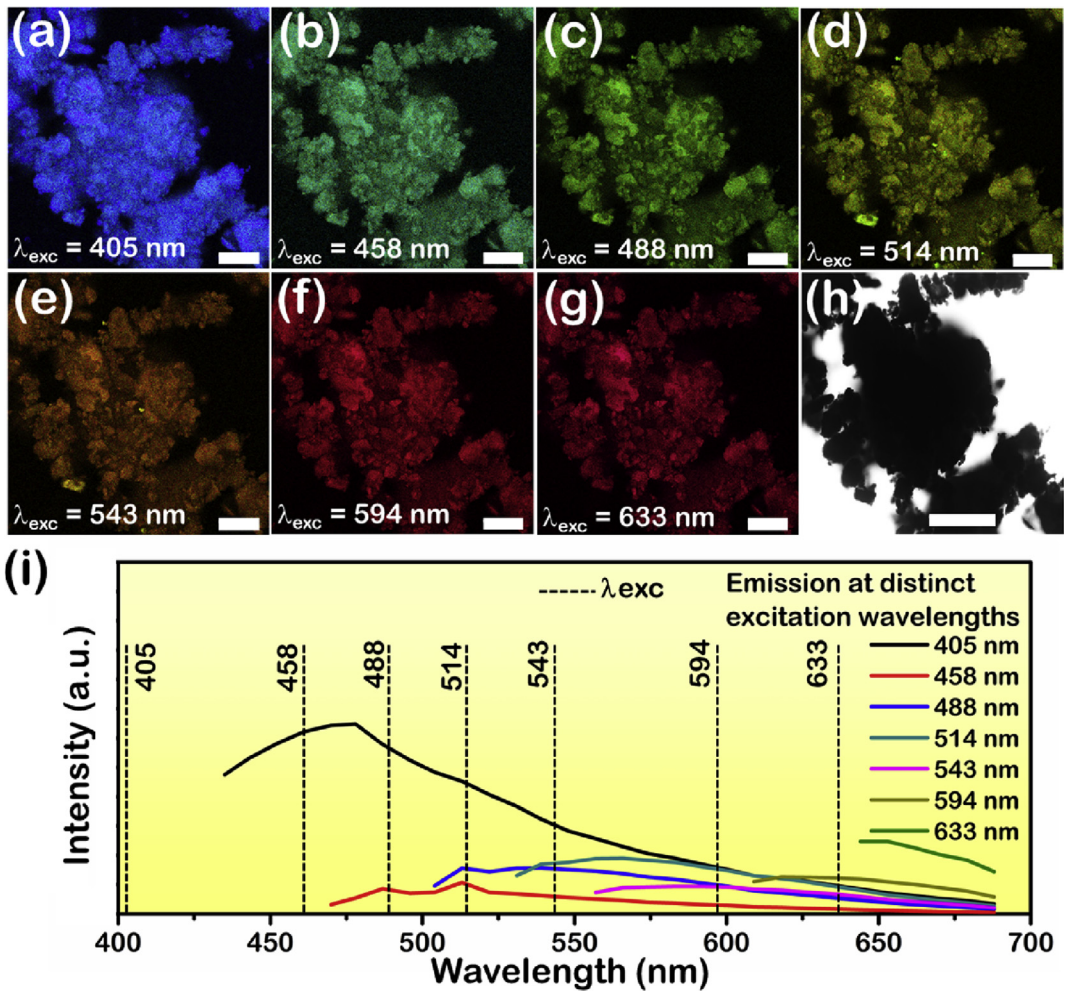

Fig. 6. Optical response of HAnr350 sample obtained by confocal microscopy. The emission image of HA were monitored by exciting at (a) $\lambda_{exc} = 405$ nm, (b) $\lambda_{exc} = 458$ nm, (c) $\lambda_{exc} = 488$ nm, (d) $\lambda_{exc} = 514$ nm, (e) $\lambda_{exc} = 543$ nm, (f) $\lambda_{exc} = 594$ nm, and (g) $\lambda_{exc} = 633$ nm. (h) Bright field micrograph of the power analyzed; scale bar = 200 μm. (i) Corresponding emission spectra obtained by exciting at the distinct wavelengths. HAnr, HA nanorod.

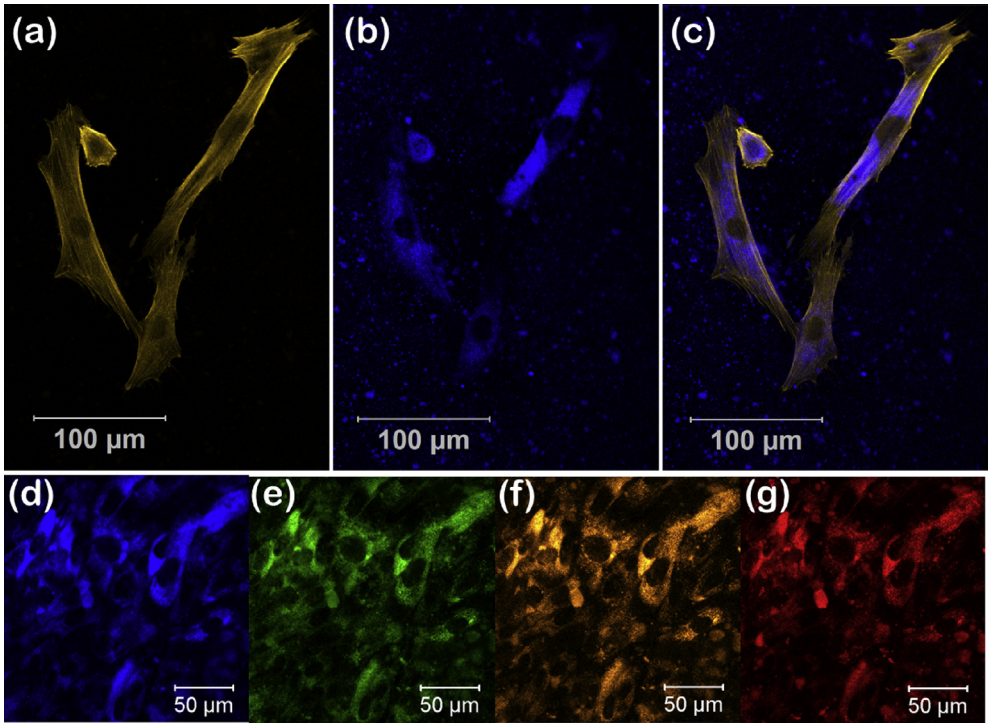

Fig. 7. Confocal imaging of HDFn cells incubated with HAnr350 sample (320 μg/mL) for 48 h. (a) Cytoskeleton labeled with Alexa Fluor 532 Phalloidin (λ_{exc} = 514 nm), (b) fluorescence image exhibiting blue fluorescent HA NPs (λ_{exc} = 405 nm), and (c) merged images. (d–g) Multiple excitation/emission imaging of intracellular HAnr350 NPs (λ_{exc} = 405, 488, 543, and 594 nm, respectively). HDFn, Human dermal fibroblast; HAnr, HA nanorod; NP, nanoparticles; HA, hydroxyapatite.

temperature increases, however, the corresponding coordinates pass from x = 0.28 and y = 0.33 (38 K) to x = 0.35 and y = 0.38 (300 K), which is a shift from bluish-to yellowish-white emission. On the other hand, excitation with a Xe lamp results in emissions from the HAnr350 sample of pure colors which dramatically change as the excitation wavelength increases, in the blue, green, yellow, and red regions. This result confirms the fully tunable multicolor behavior of the prepared HA sample.

3.3. *In vitro cytotoxicity and cell-imaging*

The evaluation of biocompatibility is crucial for future bio-applications of fluorescent HA. In this case, the *in vitro* cytotoxicity of the HAnr350 sample was evaluated by MTT assay with human cells. For this study, we selected HDFn cells as the model culture, which was incubated with HAnrs for 24 and 48 hours at different dosages of NPs (from 20 to 320 μg/mL). Fig. 5 shows the obtained results, and the analysis of the results indicates that for 24 h of incubation, no cytotoxic effects were observed, and no significant changes in viability values were evident by comparing the evaluated groups with the control group. This behavior was also observed for HA NPs over 48 h of incubation, with the exception of groups exposed to NPs solutions of 40, 80, and 320 μg/mL. In these cases, the results suggest that the HAnr350 sample may increase cell metabolism, which have to be further evaluated using alternative methodologies. A similar trend was observed by *Kumar* et al. [74], where the fluorescent HA NPs increased the growth activity of mouse fibroblast 3T3-L1 cells. Also, the images acquired by microscopy with phase contrast (Figs. S4 and S5) demonstrate that for both the 24 and 48 h groups, the presence of the NPs do not induce changes in the morphology of the cells, preserving their elongated and fusiform shape. The present results confirm the good biocompatibility of the fluorescent HAnr350 sample with potential to be applied in biomedical approaches, such as cell imaging, drug delivery, and theranostics applications.

In the present study, we probed the optimized HAnr350 sample for use as a contrast agent by its intrinsic fluorescence property. The NPs were first imaged by confocal microscope using excitation with distinct laser sources, and Fig. 6(a–h) shows the obtained results. The fluorescence images are close to identical in the excitation range 405−633 nm, and the emissive locations match well with each other, reinforcing that the tunability is intrinsically related to the HA particles. Also, the CIE chromaticity coordinates are consistent with those obtained by varying the excitation wavelength using the spectrofluorometer (see Tables S2 and S3, and Fig. S3). The NPs are detectable by imaging and exhibit significant fluorescence intensity using distinct energies of excitation (Fig. 6(i)). This result demonstrates the potential for use in multicolor and multimodal imaging applications and for procedures with concomitant use of distinct fluorescent probes. The excitation-dependent fluorescence is very promising and still needs to be explored further. The present work represents a preliminary step to demonstrating the preparation of full-color tunable HA NPs.

Considering the low cytotoxicity and the optimal region for excitation of our sample to obtain the highest fluorescence intensity, we probed the HAnr350 sample for cell imaging by confocal microscopy at λ_{exc} = 405 nm. By obtaining images at a single location, this technique allows the acquisition of images in thicker samples, avoiding interference from scattered light. By using biolabels, it is possible to differentiate structures and mechanisms in cells [81,82]. Fig. 7(a–c) shows bioimaging and uptake probes using HDFn cells incubated with 320 μg/mL of HAnr350 NPs for 48 h. For these probes, Alexa Fluor 532 Phalloidin was used to label the cytoskeleton of cells to better demonstrate the internalization of the NPs. As shown in Fig. 7(a), the labeling procedure with Phalloidin was specific, leading to a yellow emission by excitation at

514 nm, and the presence of HAnr350 did not show any interference with the labeling procedure, evidencing its capability to be used with other biolabeling compounds. Moreover, the low intensity at the central region of the cells reveals the localization of the nucleus.

By changing the irradiation source for excitation at 405 nm, the bright blue fluorescence of HAnr350 is detected, as shown in Fig. 7(b). The delimitation of cells and their cytoplasm is evidenced as well as the nucleus structure, as observed by the lower fluorescence of the NPs in this region. These results confirm that the HAnr350 NPs are localized in the cytosol region and are not just their presence at the membrane surface. Also, some aggregates of NPs outside the HDFn cells are observed, suggesting that the NPs are only partially eliminated by the washing step. The homogeneous fluorescence inside the cells reveals that only the well-dispersed NPs are uptaken. Fig. 7(c) shows the superimposition of both Phalloidin and HAnr350 fluorescence which demonstrates that the NPs were successfully internalized by cells and that the NPs are more localized at regions near the nucleus structure. The endoplasmic reticulum consists of an organelle intrinsically associated with the nuclear envelope and could be a target for NPs [83]. From these results, it is also important to emphasize that cell morphology remains undamaged after uptake of the HAnr350 sample even after long-time incubation (48 h), corroborating the MTT results that suggest high biocompatibility of the NPs.

The suitability of the samples was also probed for multicolor cell-imaging. As shown in Fig. 7(d–g), when intracellular HAnr350 NPs are imaged at $\lambda_{exc} = 405$, 488, 543, and 594 nm, intense fluorescence emissions of blue, green, yellow, and red colors are respectively observed in HDFn cells. This result is consistent with the excitation-dependent fluorescence shown in Figs. 4 and 6. Hence, the present study demonstrates a possible application for the novel heat-treated HAnrs as a new non-toxic and multicolor biolabeling probe in fluorescence imaging procedures because of its self-activated luminescence property.

4. Conclusions

In summary, we have demonstrated that HAnrs obtained by a simple strategy, based on chemical precipitation followed by heat treatment at a relatively low temperature (350°C) display intense and tunable fluorescence emissions. The emission colors of HA change from blue to red and also white colors, depending on the temperature, the source of optical measurements, and the excitation wavelengths. This behavior is attributed to structural order-disorder effects induced by defects, including impurities (CO_3^{2-}, H_2O, and NH_4^+), distortions in structural clusters, and vacancies (Ca, OH). The elimination/decomposition of impurities trapped in the HA lattice greatly improves the radiative recombination of e'–$h^\bullet$ pairs between defect-related energy levels. Hence, HAnrs are made up of earth-abundant elements with low toxicity and present self-activated fluorescence avoiding the use of lanthanide dopants or coupling the NPs with organic dyes. The heat-treated material has good biocompatibility and can be internalized in human cells without any evident cellular damage. The present study demonstrated by confocal imaging that this novel form of HA is a potential non-toxic and multicolor fluorescent probe in future clinical applications for cell imaging procedures.

Data availability

The raw/processed data required to reproduce these findings cannot be shared at this time because of technical or time limitations.

Author contributions

The manuscript was written with contributions of all authors. All authors have given approval to the final version of the manuscript.

Conflict of interest

The authors declare that they have no known competing financial interests or personal relationships that could have appeared to influence the work reported in this article.

Acknowledgments

The authors acknowledge the financial support of the following agencies: Coordenação de Aperfeiçoamento de Pessoal de Nível Superior—Brazil (CAPES), Financial Code 001, PNPD Program. The authors also thank FAPESP (Grants 2013/11144-3, 2013/07296-2, 2013/07276-1 and 2009/54035-4) and CNPq (Grants 141964/2018-9). Authors are grateful to Generalitat Valenciana for PrometeoII/2014/022 (J.A.) and for ACOMP/2015/1202 (J.A.), to Universitat Jaume I for projects UJI-B2016-25 (J.A.) and UJI-B2016-38 (H.B-M. and E.C.) and to the Ministerio de Economía y Competitividad (Spain) for projects CTQ2015-65207-P (J.A.) and MAT2016-80410-P (H.B-M. and E.C.). The authors thank Enio Longo for the support with the scientific illustrations and Rori Camargo for electron microscopy images. Special thanks to Prof. Francisco Guimarães and Prof. Valmor Mastelaro for the support with confocal microscopy and XPS analyses, respectively.

Appendix A. Supplementary data

Supplementary data to this article can be found online at https://doi.org/10.1016/j.mtchem.2019.100211.

References

[1] V. Ntziachristos, Fluorescence molecular imaging, Annu. Rev. Biomed. Eng. 8 (2006) 1–33, https://doi.org/10.1146/annurev.bioeng.8.061505.095831.
[2] O.S. Wolfbeis, An overview of nanoparticles commonly used in fluorescent bioimaging, Chem. Soc. Rev. 44 (2015) 4743–4768, https://doi.org/10.1039/C4CS00392F.
[3] Z. Yang, S.M. Usama, F. Li, K. Burgess, Z. Li, A zwitterionic near-infrared dye linked TrkC targeting agent for imaging metastatic breast cancer, Medchemcomm 9 (2018) 1754–1760, https://doi.org/10.1039/c8md00190a.
[4] M. Chen, M. Yin, Design and development of fluorescent nanostructures for bioimaging, Prog. Polym. Sci. 39 (2014) 365–395, https://doi.org/10.1016/j.progpolymsci.2013.11.001.
[5] Q. Zhan, J. Qian, H. Liang, G. Somesfalean, D. Wang, S. He, Z. Zhang, S. Andersson-Engels, Using 915 nm laser excited Tm^{3+}/Ho^{3+}-doped $NaYbF_4$ upconversion nanoparticles for in vitro and deeper in vivo bioimaging without overheating irradiation, ACS Nano 5 (2011) 3744–3757, https://doi.org/10.1021/nn200110j.
[6] F. Wang, X. Xue, X. Liu, Multicolor tuning of (Ln,P)-doped YVO_4 nanoparticles by single-wavelength excitation, Angew. Chem. Int. Ed. 47 (2008) 906–909, https://doi.org/10.1002/anie.200704520.
[7] D. Yan, B. Lei, B. Chen, X.J. Wu, Z. Liu, N. Li, J. Ge, Y. Xue, Y. Du, Z. Zheng, H. Zhang, Synthesis of high-quality lanthanide oxybromides nanocrystals with single-source precursor for promising applications in cancer cells imaging, Appl. Mater. Today. 1 (2015) 20–26, https://doi.org/10.1016/j.apmt.2015.06.001.
[8] Y. Song, S. Zhu, B. Yang, Bioimaging based on fluorescent carbon dots, RSC Adv. 4 (2014) 27184–27200, https://doi.org/10.1039/c3ra47994c.
[9] S. Aiyer, R. Prasad, M. Kumar, K. Nirvikar, B. Jain, O.S. Kushwaha, Fluorescent carbon nanodots for targeted in vitro cancer cell imaging, Appl. Mater. Today. 4 (2016) 71–77, https://doi.org/10.1016/j.apmt.2016.07.001.
[10] E. Boisselier, D. Astruc, Gold nanoparticles in nanomedicine: preparations, imaging, diagnostics, therapies and toxicity, Chem. Soc. Rev. 38 (2009) 1759–1782, https://doi.org/10.1039/b806051g.
[11] R.B.P. Elmes, K.N. Orange, S.M. Cloonan, D.C. Williams, T. Gunnlaugsson, Luminescent ruthenium(II) polypyridyl functionalized gold nanoparticles; their DNA binding abilities and application as cellular imaging agents, J. Am. Chem. Soc. 133 (2011) 15862–15865, https://doi.org/10.1021/ja2061159.

[12] F. Zhang, G.B. Braun, Y. Shi, Y. Zhang, X. Sun, N.O. Reich, D. Zhao, G. Stucky, Fabrication of Ag@SiO_2@Y_2O_3:Er nanostructures for bioimaging: tuning of the upconversion fluorescence with silver nanoparticles, J. Am. Chem. Soc. 132 (2010) 2850–2851.

[13] Y. Li, Y. Guo, J. Ge, P.X. Ma, B. Lei, In situ silica nanoparticles-reinforced biodegradable poly(citrate-siloxane) hybrid elastomers with multifunctional properties for simultaneous bioimaging and bone tissue regeneration, Appl. Mater. Today. 10 (2018) 153–163, https://doi.org/10.1016/j.apmt.2017.11.007.

[14] F. Perton, M. Tasso, G. Muñoz-Medina, M. Ménard, C. Blanco-Andujar, E. Portiansky, M. Fernandez van Raap, D. Bégin, F. Meyer, S. Bégin-Colin, D. Mertz, Fluorescent and magnetic stellate mesoporous silica for bimodal imaging and magnetic hyperthermia, Appl. Mater. Today. 16 (2019) 301–314, https://doi.org/10.1016/j.apmt.2019.06.006.

[15] N. Erathodiyil, J.Y. Ying, Functionalization of inorganic nanoparticles for bioimaging applications, Acc. Chem. Res. 44 (2011) 925–935, https://doi.org/10.1021/ar2000327.

[16] V.M. Ozhukil, V.K. Pillai, S. Alwarappan, Spotlighting graphene quantum dots and beyond: synthesis, properties and sensing applications, Appl. Mater. Today. 9 (2017) 350–371, https://doi.org/10.1016/j.apmt.2017.09.002.

[17] Z. Yang, L. Deng, Y. Lan, X. Zhang, Z. Gao, C. Chu, D. Cai, Z. Ren, Molecular extraction in single live cells by sneaking in and out magnetic nanomaterials, Proc. Natl. Acad. Sci. 111 (2014) 10966–10971, https://doi.org/10.1073/pnas.1411802111.

[18] J. Yao, M. Yang, Y. Duan, Chemistry, biology, and medicine of fluorescent nanomaterials and related systems: new insights into biosensing, bioimaging, genomics, diagnostics, and therapy, Chem. Rev. 114 (2014) 6130–6178, https://doi.org/10.1021/cr200359p.

[19] C. Qi, J. Lin, L.H. Fu, P. Huang, Calcium-based biomaterials for diagnosis, treatment, and theranostics, Chem. Soc. Rev. 47 (2018) 357–403, https://doi.org/10.1039/c6cs00746e.

[20] S.V. Dorozhkin, Nanosized and nanocrystalline calcium orthophosphates, Acta Biomater. 6 (2010) 715–734, https://doi.org/10.1016/j.actbio.2009.10.031.

[21] M. Vallet-Regí, J.M. González-Calbet, Calcium phosphates as substitution of bone tissues, Prog. Solid State Chem. 32 (2004) 1–31, https://doi.org/10.1016/j.progsolidstchem.2004.07.001.

[22] J.M. Bouler, P. Pilet, O. Gauthier, E. Verron, Biphasic calcium phosphate ceramics for bone reconstruction: a review of biological response, Acta Biomater. 53 (2017) 1–12, https://doi.org/10.1016/j.actbio.2017.01.076.

[23] Y. Zhou, Y. Zhou, L. Gao, C. Wu, J. Chang, Synthesis of artificial dental enamel by an elastin-like polypeptide assisted biomimetic approach, J. Mater. Chem. B. 6 (2018) 844–853, https://doi.org/10.1039/c7tb02576a.

[24] S.P. Victor, M.G. Gayathri-Devi, W. Paul, V.M. Vijayan, J. Muthu, C.P. Sharma, Europium doped calcium deficient hydroxyapatite as theranostic nanoplatforms: effect of structure and aspect ratio, ACS Biomater. Sci. Eng. 3 (2017) 3588–3595, https://doi.org/10.1021/acsbiomaterials.7b00453.

[25] S.S. Syamchand, G. Sony, Multifunctional hydroxyapatite nanoparticles for drug delivery and multimodal molecular imaging, Microchim. Acta. 182 (2015) 1567–1589, https://doi.org/10.1007/s00604-015-1504-x.

[26] P. Yang, Z. Quan, C. Li, X. Kang, H. Lian, J. Lin, Bioactive, luminescent and mesoporous europium-doped hydroxyapatite as a drug carrier, Biomaterials 29 (2008) 4341–4347, https://doi.org/10.1016/j.biomaterials.2008.07.042.

[27] M. Kester, Y. Heakal, T. Fox, A. Sharma, G.P. Robertson, T.T. Morgan, E.I. Altinoğlu, A. Tabaković, M.R. Parette, S.M. Rouse, V. Ruiz-Velasco, J.H. Adair, Calcium phosphate nanocomposite particles for in vitro imaging and encapsulated chemotherapeutic drug delivery to cancer cells, Nano Lett. 8 (2008) 4116–4121, https://doi.org/10.1021/nl802098g.

[28] S.P. Victor, W. Paul, M. Jayabalan, C.P. Sharma, Supramolecular hydroxyapatite complexes as theranostic near-infrared luminescent drug carriers, CrystEngComm 16 (2014) 9033–9042, https://doi.org/10.1039/c4ce01137f.

[29] B.M. Barth, R. Sharma, E.I. Altinoglu, T.T. Morgan, S.S. Shanmugavelandy, J.M. Kaiser, C. Mcgovern, G.L. Matters, J.P. Smith, M. Kester, J.H. Adair, Bioconjugation of calcium phosphosilicate composite nanoparticles and pancreatic cancers in vivo, ACS Nano 4 (2010) 1279–1287, https://doi.org/10.1021/nn901297q.

[30] E.I. Antinoglu, T.J. Russin, J.M. Kaiser, B.M. Barth, P.C. Eklund, M. Kester, J.H. Adair, Near-infrared emitting fluorophore-doped calcium phosphate nanoparticles for in vivo imaging of human breast cancer, ACS Nano 2 (2008) 2075–2084, https://doi.org/10.1021/nn800448r.

[31] Y. Xie, W. He, F. Li, T.S.H. Perera, L. Gan, Y. Han, X. Wang, S. Li, H. Dai, Luminescence enhanced Eu^{3+}/Gd^{3+} co-doped hydroxyapatite nanocrystals as imaging agents in vitro and in vivo, ACS Appl. Mater. Interfaces 8 (2016) 10212–10219, https://doi.org/10.1021/acsami.6b01814.

[32] B. Ma, S. Zhang, J. Qiu, J. Li, Y. Sang, H. Xia, H. Jiang, J. Claverie, H. Liu, Eu/Tb codoped spindle-shaped fluorinated hydroxyapatite nanoparticles for dual-color cell imaging, Nanoscale 8 (2016) 11580–11587, https://doi.org/10.1039/c6nr02137a.

[33] X. Zheng, M. Liu, J. Hui, D. Fan, H. Ma, X. Zhang, Y. Wang, Y. Wei, Ln^{3+}-doped hydroxyapatite nanocrystals: controllable synthesis and cell imaging, Phys. Chem. Chem. Phys. 17 (2015) 20301–20307, https://doi.org/10.1039/c5cp01845e.

[34] D.E. Wagner, K.M. Eisenmann, A.L. Nestor-Kalinoski, S.B. Bhaduri, A microwave-assisted solution combustion synthesis to produce europium-doped calcium phosphate nanowhiskers for bioimaging applications, Acta Biomater. 9 (2013) 8422–8432, https://doi.org/10.1016/j.actbio.2013.05.033.

[35] A. Escudero, M.E. Calvo, S. Rivera-Fernández, J.M. De La Fuente, M. Ocaña, Microwave-assisted synthesis of biocompatible europium-doped calcium hydroxyapatite and fluoroapatite luminescent nanospindles functionalized with poly(acrylic acid), Langmuir 29 (2013) 1985–1994, https://doi.org/10.1021/la304534f.

[36] J. Hui, X. Zhang, Z. Zhang, S. Wang, L. Tao, Y. Wei, X. Wang, Fluoridated HAp: Ln^{3+} (Ln = Eu or Tb) nanoparticles for cell-imaging, Nanoscale 4 (2012) 6967–6970, https://doi.org/10.1039/c2nr32404k.

[37] A. Doat, M. Fanjul, F. Pellé, E. Hollande, A. Lebugle, Europium-doped bioapatite: a new photostable biological probe, internalizable by human cells, Biomaterials 24 (2003) 3365–3371, https://doi.org/10.1016/S0142-9612(03)00169-8.

[38] Y. Guo, D. Shi, J. Lian, Z. Dong, W. Wang, H. Cho, G. Liu, L. Wang, R.C. Ewing, Quantum dot conjugated hydroxylapatite nanoparticles for in vivo imaging, Nanotechnology 19 (2008) 175102, https://doi.org/10.1088/0957-4484/19/17/175102.

[39] Y. Zhao, L. Shi, J. Fang, X. Feng, Bio-nanoplatforms based on carbon dots conjugating with F-substituted nano-hydroxyapatite for cellular imaging, Nanoscale 7 (2015) 20033–20041, https://doi.org/10.1039/c5nr06837a.

[40] M. Liu, H. Liu, S. Sun, X. Li, Y. Zhou, Z. Hou, J. Lin, Multifunctional hydroxyapatite/Na(Y/Gd)F_4:Yb^{3+},Er^{3+} composite fibers for drug delivery and dual modal imaging, Langmuir 30 (2014) 1176–1182, https://doi.org/10.1163/9789004218642.

[41] C. Eggeling, J. Widengren, R. Rigler, C.A.M. Seidel, Photobleaching of fluorescent dyes under conditions used for single-molecule detection: evidence of two-step photolysis, Anal. Chem. 70 (1998) 2651–2659, https://doi.org/10.1021/ac980027p.

[42] F. Xie, T.A. Zhang, D. Dreisinger, F. Doyle, A critical review on solvent extraction of rare earths from aqueous solutions, Miner. Eng. 56 (2014) 10–28, https://doi.org/10.1016/j.mineng.2013.10.021.

[43] A. Tabaković, M. Kester, J.H. Adair, Calcium phosphate-based composite nanoparticles in bioimaging and therapeutic delivery applications, WIREs Nanomed, Nanobiotechnol 4 (2012) 96–112, https://doi.org/10.1002/wnan.163.

[44] S.K. Gupta, P.S. Ghosh, N. Pathak, R. Tewari, Nature of defects in blue light emitting $CaZrO_3$: spectroscopic and theoretical study, RSC Adv. 5 (2015) 56526–56533, https://doi.org/10.1039/C5RA09637E.

[45] C. Zhang, J. Lin, Defect-related luminescent materials: synthesis, emission properties and applications, Chem. Soc. Rev. 41 (2012) 7938–7961, https://doi.org/10.1039/c2cs35215j.

[46] B. Wopenka, J.D. Pasteris, A mineralogical perspective on the apatite in bone, Mater. Sci. Eng. C 25 (2005) 131–143, https://doi.org/10.1016/j.msec.2005.01.008.

[47] V. Uskoković, The role of hydroxyl channel in defining selected physicochemical peculiarities exhibited by hydroxyapatite, RSC Adv. 5 (2015) 36614–36633, https://doi.org/10.1039/c4ra17180b.

[48] C. Wang, D. Liu, C. Zhang, J. Sun, W. Feng, X.J. Liang, S. Wang, J. Zhang, Defect-related luminescent hydroxyapatite-enhanced osteogenic differentiation of bone mesenchymal stem cells via an ATP-induced cAMP/PKA pathway, ACS Appl. Mater. Interfaces 8 (2016) 11262–11271, https://doi.org/10.1021/acsami.6b01103.

[49] W. Yang, J. Luo, M. Qi, M. Yang, Analytical methods detection of alkaline phosphatase activity and inhibition with fluorescent hydroxyapatite nanoparticles, Anal. Methods. 11 (2019) 2272–2276, https://doi.org/10.1039/c9ay00176j.

[50] S.Y. Park, K. Il Kim, S.P. Park, J.H. Lee, H.S. Jung, Aspartic acid-assisted synthesis of multifunctional strontium-substituted hydroxyapatite microspheres, Cryst. Growth Des. 16 (2016) 4318–4326, https://doi.org/10.1021/acs.cgd.6b00420.

[51] R.K. Singh, T.H. Kim, K.D. Patel, J.-J. Kim, H.-W. Kim, Development of biocompatible apatite nanorod-based drug-delivery system with in situ fluorescence imaging capacity, J. Mater. Chem. B. 2 (2014) 2039–2050, https://doi.org/10.1039/c3tb21156h.

[52] C. Zhang, C. Li, S. Huang, Z. Hou, Z. Cheng, P. Yang, C. Peng, J. Lin, Self-activated luminescent and mesoporous strontium hydroxyapatite nanorods for drug delivery, Biomaterials 31 (2010) 3374–3383, https://doi.org/10.1016/j.biomaterials.2010.01.044.

[53] C. Zhang, J. Yang, Z. Quan, P. Yang, C. Li, Z. Hou, J. Lin, Hydroxyapatite nano- and microcrystals with multiform morphologies: controllable synthesis and luminescence properties, Cryst, Growth Des. 9 (2009) 2725–2733, https://doi.org/10.1021/cg801353n.

[54] K. Deshmukh, M.M. Shaik, S.R. Ramanan, M. Kowshik, Self-activated fluorescent hydroxyapatite nanoparticles: a promising agent for bioimaging and biolabeling, ACS Biomater. Sci. Eng. 2 (2016) 1257–1264, https://doi.org/10.1021/acsbiomaterials.6b00169.

[55] C. Zhang, C. Li, J. Yang, Z. Cheng, Z. Hou, Y. Fan, J. Lin, Tunable luminescence in monodisperse zirconia spheres, Langmuir 25 (2009) 7078–7083, https://doi.org/10.1021/la900146y.

[56] Y. Xiu, Q. Gao, G.D. Li, K.X. Wang, J.S. Chen, Preparation and tunable photoluminescence of carbogenic nanoparticles confined in a microporous magnesium-aluminophosphate, Inorg. Chem. 49 (2010) 5859–5867, https://doi.org/10.1021/ic1000039.

[57] G. Gonzalez, C. Costa-Vera, L.J. Borrero, D. Soto, L. Lozada, J.I. Chango, J.C. Diaz, L. Lascano, Effect of carbonates on hydroxyapatite self-activated photoluminescence response, J. Lumin. 195 (2018) 385–395, https://doi.org/10.1016/j.jlumin.2017.11.058.
[58] T.R. Machado, J.C. Sczancoski, H. Beltrán-Mir, I.C. Nogueira, M.S. Li, J. Andrés, E. Cordoncillo, E. Longo, A novel approach to obtain highly intense self-activated photoluminescence emissions in hydroxyapatite nanoparticles, J. Solid State Chem. 249 (2017) 64–69, https://doi.org/10.1016/j.jssc.2016.12.018.
[59] T.R. Machado, J.C. Sczancoski, H. Beltrán-Mir, M.S. Li, J. Andrés, E. Cordoncillo, E. Leite, E. Longo, Structural properties and self-activated photoluminescence emissions in hydroxyapatite with distinct particle shapes, Ceram. Int. 44 (2018) 236–245, https://doi.org/10.1016/j.ceramint.2017.09.164.
[60] K. Sudarsanan, R.A. Young, Significant precision in crystal structural details. Holly springs hydroxyapatite, Acta Crystallogr. B25 (1969) 1534–1543, https://doi.org/10.1107/S0567740869004298.
[61] A. Al-Kattan, F. Errassifi, A.M. Sautereau, S. Sarda, P. Dufour, A. Barroug, I. Dos Santos, C. Combes, D. Grossin, C. Rey, C. Drouet, Medical potentialities of biomimetic apatites through adsorption, ionic substitution, and mineral/organic associations: three illustrative examples, Adv. Biomater. 12 (2010) B224–B233, https://doi.org/10.1002/adem.200980084.
[62] B.O. Fowler, Infrared studies of apatites. I. Vibrational assignments for calcium, strontium, and barium hydroxyapatites utilizing isotopic substitution, Inorg. Chem. 13 (1974) 194–207, https://doi.org/10.1021/ic50131a039.
[63] S. Marković, L. Veselinović, M.J. Lukić, L. Karanović, I. Bračko, N. Ignjatović, D. Uskoković, Synthetical bone-like and biological hydroxyapatites: a comparative study of crystal structure and morphology, Biomed. Mater. 6 (2011), 045005, https://doi.org/10.1088/1748-6041/6/4/045005.
[64] S. Raynaud, E. Champion, D. Bernache-Assollant, P. Thomas, Calcium phosphate apatites with variable Ca/P atomic ratio I. Synthesis, characterisation and thermal stability of powders, Biomaterials 23 (2002) 1065–1072, https://doi.org/10.1587/transcom.2016EBP3145.
[65] S. Kačiulis, G. Mattogno, L. Pandolfi, M. Cavalli, G. Gnappi, A. Montenero, XPS study of apatite-based coatings prepared by sol–gel technique, Appl. Surf. Sci. 151 (1999) 1–5, https://doi.org/10.1016/S0169-4332(99)00267-6.
[66] J.L. Xu, K.A. Khor, Chemical analysis of silica doped hydroxyapatite biomaterials consolidated by a spark plasma sintering method, J. Inorg. Biochem. 101 (2007) 187–195, https://doi.org/10.1016/j.jinorgbio.2006.09.030.
[67] J.C. Elliot, Structure and Chemistry of the Apatites and Other Calcium Orthophosphates, Elsevier, Amsterdam, 1994.
[68] Z.Z. Zyman, D.V. Rokhmistrov, V.I. Glushko, I.G. Ivanov, Thermal impurity reactions and structural changes in slightly carbonated hydroxyapatite, J. Mater. Sci. Mater. Med. 20 (2009) 1389–1399, https://doi.org/10.1007/s10856-009-3706-4.
[69] K. Tõnsuaadu, K.A. Gross, L. Pluduma, M. Veiderma, A review on the thermal stability of calcium apatites, J. Therm. Anal. Calorim. 110 (2012) 647–659, https://doi.org/10.1007/s10973-011-1877-y.
[70] D. Aronov, M. Chaikina, J. Haddad, A. Karlov, G. Mezinskis, L. Oster, I. Pavlovska, G. Rosenman, Electronic states spectroscopy of hydroxyapatite ceramics, J. Mater. Sci. Mater. Med. 18 (2007) 865–870, https://doi.org/10.1007/s10856-006-0080-3.
[71] K. Matsunaga, A. Kuwabara, First-principles study of vacancy formation in hydroxyapatite, Phys. Rev. B Condens. Matter Mater. Phys. 75 (2007) 1–9, https://doi.org/10.1103/PhysRevB.75.014102.
[72] V.S. Bystrov, J. Coutinho, A.V. Bystrova, Y.D. Dekhtyar, R.C. Pullar, A. Poronin, E. Palcevskis, A. Dindune, B. Alkan, C. Durucan, E.V. Paramonova, Computational study of hydroxyapatite structures, properties and defects, J. Phys. D Appl. Phys. 48 (2015) 195302, https://doi.org/10.1088/0022-3727/48/19/195302.
[73] A.V. Bystrova, Y.D. Dekhtyar, A.I. Popov, J. Coutinho, V.S. Bystrov, Modeling and synchrotron data analysis of modified hydroxyapatite structure, Ferroelectrics 475 (2015) 135–147, https://doi.org/10.17537/2014.9.171.
[74] G.S. Kumar, E.K. Girija, Flower-like hydroxyapatite nanostructure obtained from eggshell: a candidate for biomedical applications, Ceram. Int. 39 (2013) 8293–8299, https://doi.org/10.1016/j.ceramint.2013.03.099.
[75] C. Zollfrank, L. Mu, P. Greil, F.A. Mu, Photoluminescence of annealed biomimetic apatites, Acta Biomater. 1 (2005) 663–669, https://doi.org/10.1016/j.actbio.2005.06.004.
[76] B.H. Zeng, G. Duan, Y. Li, S. Yang, X. Xu, W. Cai, Blue luminescence of ZnO nanoparticles based on non-equilibrium processes: defect origins and emission controls, Adv. Funct. Mater. 20 (2010) 561–572, https://doi.org/10.1002/adfm.200901884.
[77] S.K. Gupta, K. Sudarshan, P.S. Ghosh, S. Mukherjee, R.M. Kadam, Doping-induced room temperature stabilization of metastable β-Ag_2WO_4 and origin of visible emission in α- and β-Ag_2WO_4: low temperature photoluminescence studies, J. Phys. Chem. C 120 (2016) 7265–7276, https://doi.org/10.1021/acs.jpcc.6b00078.
[78] Y. Lee, H. Teng, C. Hu, S. Hu, Temperature-dependent photoluminescence in $NaTaO_3$ with different crystalline structures, Electrochem. Solid State Lett. 11 (2008) P1–P4, https://doi.org/10.1149/1.2817476.
[79] S. Zhu, Q. Meng, L. Wang, J. Zhang, Y. Song, H. Jin, K. Zhang, H. Sun, H. Wang, B. Yang, Highly photoluminescent carbon dots for multicolor patterning, sensors, and bioimaging, Angew. Chem. Int. Ed. 52 (2013) 3953–3957, https://doi.org/10.1002/anie.201300519.
[80] B. Ma, S. Zhang, R. Liu, J. Qiu, L. Zhao, S. Wang, J. Li, Y. Sang, H. Jiang, H. Liu, Prolonged fluorescence lifetime of carbon quantum dots by combining with hydroxyapatite nanorods for bio-applications, Nanoscale 9 (2017) 2162–2171, https://doi.org/10.1039/c6nr05983j.
[81] G. Bkaily, D. Jacques, P. Pothier, Use of confocal microscopy to investigate cell structure and function, Methods Enzymol. 307 (1999) 119–135, https://doi.org/10.1007/978-90-481-2888-4.
[82] D.J. Stephens, V.J. Allan, Light microscopy techniques for live cell imaging, Science 300 (2003) 82–86, https://doi.org/10.1126/science.1082160.
[83] R. Chen, L. Huo, X. Shi, R. Bai, Z. Zhang, Y. Zhao, Y. Chang, C. Chen, Endoplasmic reticulum stress induced by zinc oxide nanoparticles is an earlier biomarker for nanotoxicological evaluation, ACS Nano 8 (2014) 2562–2574, https://doi.org/10.1021/nn406184r.